Journal of the European Ceramic Society 38 (2018) 1143–1151

Contents lists available at ScienceDirect

Journal of the European Ceramic Society

journal homepage: www.elsevier.com/locate/jeurceramsoc

Original Article

A corrosion mechanism of titanium diboride in $KF-AlF_3-Al_2O_3$ melt

Martin Kontrík[a], František Šimko[a,*], Dagmar Galusková[b], Martin Nosko[c], Valéria Bizovská[a], Michal Hičák[a], Dušan Galusek[b], Aydar Rakhmatullin[d], Michal Korenko[a]

[a] Institute of Inorganic Chemistry, Slovak Academy of Science, Dúbravská cesta 9, 845 36, Bratislava 45, Slovak Republic
[b] Vitrum Laugaricio, Joint Glass Center of the Institute of Inorganic Chemistry, Slovak Academy of Sciences, Alexander Dubček University of Trenčín and Faculty of Chemical and Food Technology, Slovak University of Technology, Študentská 2, 911 50, Trenčín, Slovak Republic
[c] Institute of Materials and Machine Mechanics, Slovak Academy of Science, Dúbravská cesta 9, 845 13, Bratislava, Slovak Republic
[d] CNRS, CEMHTI UPR3079, Univ. Orléans, F-45071 Orléans, France

ARTICLE INFO

Keywords:
Titanium diboride
Fluoride
Molten salt
Corrosion
Mullite type structure

ABSTRACT

TiB_2 samples were exposed to molten $KF-AlF_3-Al_2O_3$: 54.8-42.1-3.1 mol% salt, at 680 °C for 50, 100 and 200 h. The corroded samples of TiB_2 were investigated by SEM-EDX, EBSD, XRD, FT-IR and MAS NMR analysis. Corrosion was noted to occur predominantly as pitting attacks on the surface of the investigated materials. An inter-crystal and *trans*-crystal corrosion were identified on the cross-sections of the samples. A perturbation of Ti−B bonds was detected (SEM-EDX and NMR analysis), at which a formation of orthorhombic TiO_2 was also identified (EBSD analysis). The subsequent NMR, XRD and FT-IR analysis of the behaviour of TiB_2 powder in molten $KF-AlF_3-Al_2O_3$ supports the statement about the formation of orthorhombic TiO_2 and mullite type of aluminium borates.

1. Introduction

One of the major limiting factors in industrial applications of any structural material is its corrosion behaviour. This is quite evident for fluoride salt systems, at high temperatures, in particular. The largest industrial application of molten fluoride salts is, by far, aluminium electrolysis (Hall-Héroult process). The Hall-Héroult process reduces the alumina to aluminium in electrolytic cell. Alumina is, in Hall-Héroult process, dissolved in an electrolyte consisting mainly of liquid cryolite (Na_3AlF_6). The electrolyte is modified by several additives in order to control its physico-chemical parameters, like melting point, electrical conductivity, density, viscosity, etc. In modern alumina reduction cell, several pre-baked anodes discharge oxide ions from dissolved alumina, and gradually consume themselves, forming gaseous CO_2 [1].

A newly proposed, eco-economic way, for aluminium production, based on the inert electrode system (for both, cathode and anode) is expected to change current production process and make energy savings by a large margin at the zero emissions of CO_2 [1]. As an important component of the inert electrode system, the wettable cathodes could have had an impact on the commercial promotion of this inert electrode system. The Gibbs free energies calculations determine titanium diboride (TiB_2) to be the candidate material for such a wettable inert cathode system [2]. TiB_2 is also regarded as ideal for aluminium reduction cells because of its excellent properties like electrical conductivity (9–15 × 10^5 S/cm), wettability with molten aluminium and low solubility in aluminium (0.25 mm/year) [3]. Newly developed methods of its synthesis allow preparation of this material with required properties [4,5]. (All the details of the new cathode inert technology for aluminium electrolysis could be found elsewhere) [1–6].

The stable layer of TiB_2 on the graphite substrate is responsible for higher current density at the electrolyser's bottom, higher current efficiency and, first of all, TiB_2 can substantially decrease diffusion of alkali metals to the graphite pot lining [6,7]. The last mentioned parameter is of great importance for, so-called acidic, low-melting electrolytes, systems with higher content of potassium fluoride.

These melts have much lower melting point than those used recently, based on $NaF-AlF_3$. This fact means wider variability in terms of electrolyte composition. Low temperature electrolytes are also referred to as "inert-anode friendly" electrolytes. They have lower operating temperature, which leads to lower corrosion impact of the electrolyte towards electrodes and structural materials of the cell [8–10].

The $KF-AlF_3$ based electrolytes may have decreased the temperature of the process by as much as 250 °C [11]. Recently, the research is mostly focused to find a relation between the composition of TiB_2 and its critical physical properties, like wettability, electrical conductivity and corrosive resistance towards liquid aluminium [7,12–14]. Also, we have to take into account, that a film of molten electrolyte is always

* Corresponding author at: Institute of Inorganic Chemistry, Slovak Academy of Sciences, Dúbravská cesta 9, 845 36, Bratislava, Slovakia.
E-mail address: uachsim@savba.sk (F. Šimko).

https://doi.org/10.1016/j.jeurceramsoc.2017.11.030
Received 21 September 2017; Received in revised form 10 November 2017; Accepted 12 November 2017
Available online 13 November 2017

formed on the cathode surface between the lining and molten aluminium. Therefore, the possible interaction of a cathode material with molten electrolyte should never be excluded [2]. To our knowledge, there is no work in open literature deals with the mechanism of corrosion of TiB_2 materials in molten cryolite electrolytes.

The scientific objectives of the present paper are, therefore, focused on the investigation of corrosion mechanism of TiB_2 ceramic material in $KF-AlF_3-Al_2O_3$ melt. A static corrosion tests, where TiB_2 samples were exposed to fluoride melts ($KF-AlF_3-Al_2O_3$), with the fixed composition: 54.8–42.1–3.1 mol%, were performed, at 680 °C for 50, 100 and 200 h. Corrosion products were identified by X-ray diffraction (XRD), Fourier transform infrared spectroscopy (FT-IR), Scanning electron microscopy (SEM-EDX) and Electron back-scatter diffraction (EBSD) analysis. Solidified samples of the molten salt were, after the corrosion tests, also analysed by XRD. In order to understand the corrosion mechanism, we have also analysed the solidified mixture of the fluoride melt and TiB_2 by XRD, FT-IR and by Magic angle spinning (MAS) Nuclear magnetic resonance (NMR) spectroscopy. The mixture was prepared with the higher concentration of TiB_2, that allows us to identify all the reaction products coming from the interaction between the fluorides and TiB_2.

2. Materials and experimental procedures

2.1. TiB_2 ceramic material

The static tests were performed with commercially available titanium diboride (Alluter Advanced Manufacture Ltd.) (≥98 wt.%). The supplied solid block was cut by water beam. Diamond cutting tools were used to facilitate the TiB_2 samples (dimensions 45 × 6 × 6 mm) for corrosion tests. After cutting, the samples were cleaned in ethanol (Emsure, Slovakia, 99.5%) and placed into the glove box with an inert argon atmosphere (Messer, Slovakia, 99,999%, air moisture below 10 ppm, oxygen content below 1 ppm). Before the corrosion tests, itself, the microstructure of TiB_2 material was characterized and the density and porosity were determined. The data are listed in Table 1. Both, density and porosity were determined by the Archimedean method in water at ambient temperature. Three samples taken from different parts of the original material were used for this initial characterisation. Samples were weighted in dry, soaked and immersed state. Density and porosity (open, closed and overall) were, then, calculated.

Obtained TiB_2 has quite high overall porosity (ca 6.7%). Inhomogeneity was observed, the open and closed porosity varied from place to place, as listed in Table 1. The density of the TiB_2 material ranges between 4.19 and 4.25 g × cm^{-3} (it is in a good agreement with the data provided by supplier).

The microstructure of TiB_2 material predominantly consists of spherical titanium diboride grains, the intergranular phase and pores. The average grain size is within the 25–50 μm range. The grains with the larger size (up to 100 μm) were, however, also observed. The intergranular phase primary consists of nickel, which was used as the main sintering additive. SEM-EDX analysis were used for the identification of the predominant atomic species and the elemental distribution Fig. 1.

Table 1
Density (ρ_s), open (Φ_o), closed (Φ_u) and overall (Φ_{ov}) porosity of TiB_2 samples.

Sample number	ρ_s/g–cm^{-3}	Φ_o/%	Φ_u/%	Φ_{ov}/%
1	4.22	1.2	5.5	6.7
2	4.25	0.7	5.4	6.1
3	4.19	5.3	2.1	7.4
average	4.22	2.4	4.3	6.7
supplier	4.2 ≈ 4.5	–	–	–

2.2. Corrosion tests

The corrosion medium consisting of a mixture of $KF-AlF_3-Al_2O_3$: 54.8-42.1-3.1 mol% was used for static corrosion tests. The cryolite ratio of the melt (CR, molar ratio $n(KF)/n(AlF_3)$) is 1.3. KF (Sigma-Aldrich; 99.0%), dried under vacuum at 200 °C for 24 h, AlF_3 (min. 99%), re-sublimated and Al_2O_3 (Fluka; 99.7%) were used. The preparation of the all samples were carried out in the glove box under inert, argon atmosphere (Ar, 99.999%). Weighted and cleaned samples of TiB_2 were put into sintered alumina crucibles (99.7% purity Al_2O_3) and filed up with the powdered melt. The crucibles were closed and sealed by SiO_2–Al_2O_3 paste into alumina capsules. The design of the capsules is depicted on Fig. 2.

Sealed capsule was put the resistance furnace and heated in resistance furnace under the slight overpressure of inert Argon gas (Ar, 99.999%). TiB_2 samples were exposed to molten $KF-AlF_3-Al_2O_3$: 54.87-42.1-3.1 mol% salt, at 680 °C for 50, 100 and 200 h. After the corrosion tests, the samples were removed and washed in a prepared molten $LiCl-KCl_{(eut)}$ bath mixture (Lachema, Czech Rep.; 99.8%). The temperature of the washing procedure was 600 °C, 10 min was the holding time. This melt is an effective medium for the cleaning of the surface of the samples from the fluoride residual materials [15,16]. The remaining chlorides were then removed by water and the rest of the residual solid material was finally cleansed using an ultrasonic bath (water/ethanol ≈ 10:1). After the cleaning procedure, the weight of each samples were taken. The epoxy resin (Scandiplast) was used to embed the samples for microstructure observation. The Embedded samples were then grounded and polished (Struers, Denmark; Tegra Force-5) with a diamond suspension (1 μm). After that, the final cleaning with ethanol and drying was applied.

In some samples (used for cross-section analysis), the removal of the solidified melt, described above, has not been used.

2.3. SEM-EDX and EBSD analysis

Scanning electron microscopy (SEM) (JEOL 7600F, Japan) in combination with Electron dispersive X-ray spectroscopy (EDX) (Oxford Instruments Ltd., UK) was used for the superficial and cross-sectional microstructure observation. To ensure EDX measurements accuracy, the voltage was set to 10 kV (according to Monte Carlo simulations of electron trajectory in solids via Casino v 2.48), to supress the side effects of the electron signal from the interaction volume [17]. Electron back-scatter diffraction (EBSD) (HKLNordlys, Oxford Instruments Ltd., UK) was used to assist in the SEM-EDX analysis. The samples for EBSD characterization were prepared by mechanical grinding and polishing, proceeded by final mechano-chemical polishing using colloidal silica OP-S suspension, 45 min.

2.4. XRD powder diffraction

X-ray powder diffraction patterns were collected with Empyrean X-ray diffractometer (PANalytical, Netherlands) with Cu K_α radiation in Bragg-Brentano reflection geometry, equipped with a PIXcel 3D detector. The K_β radiation was subtracted using Ni-filter. The records were taken in the 2Θ range of 10–70° with a step size 0.02° of 2Θ at room temperature and $K_{\alpha 2}$ software subtraction. Phase analysis was performed with X'Pert HighScore Plus PANanalytical software with PDF2 2014 database.

2.5. FT – IR spectroscopy

Fourier transform infrared spectra (FT-IR) were collected with spectrometer Nicolet 6700 (Thermo Scientific, USA) equipped with a KBr beam splitter and a deuterated-triglycine sulphate (DTGS) detector for the mid-infrared region (4000–350 cm^{-1}). Prior to each IR measurement the samples were stored in a desiccator above P_2O_5, for 72 h.

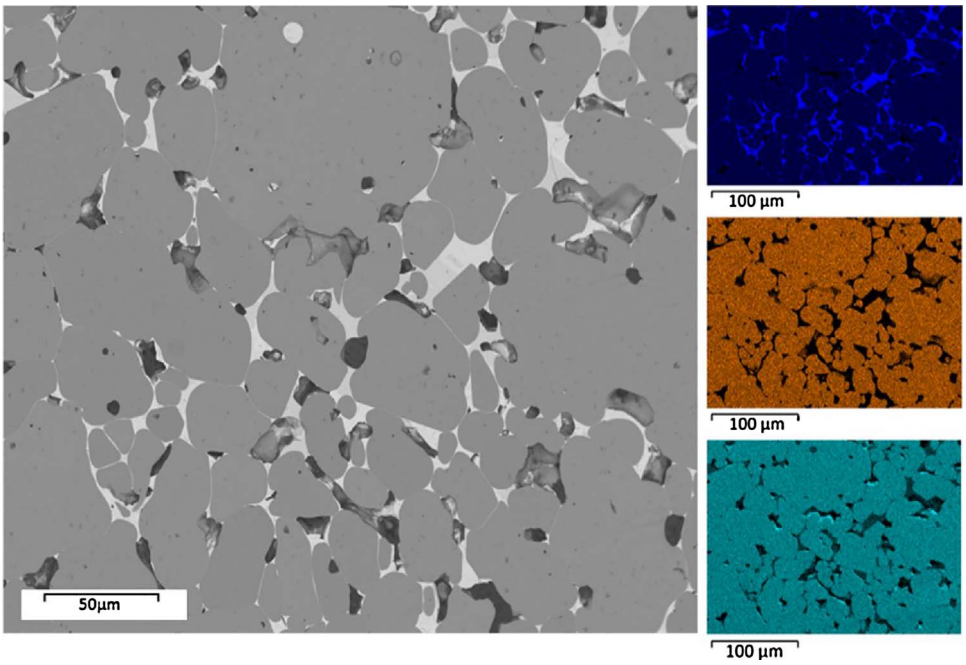

Fig. 1. Cross–section of the original (non-corroded) TiB_2 sample, SEM-EDX elemental analysis – elemental mapping: blue – Ni, orange – Ti, green – B. (For interpretation of the references to colour in this figure legend, the reader is referred to the web version of this article.)

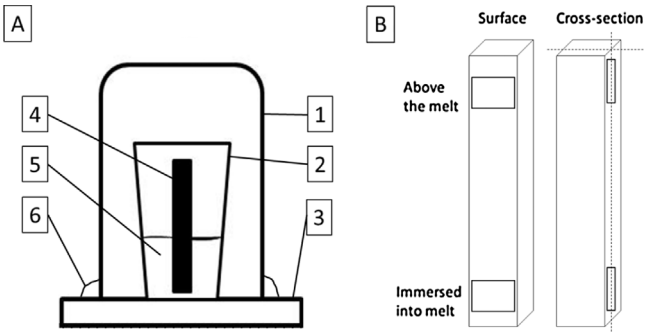

Fig. 2. A) Closed sample: 1 – Alumina capsule, 2 – Alumina crucible with melt and sample, 3 – Alumina base, 4 – sample, 5 – corrosion medium, 6 – SiO_2–Al_2O_3 paste; B) Analysed areas.

To obtain spectra in the MIR region the KBr pressed disk technique (1 mg of sample and 200 mg of KBr) was used. Thermo Scientific OMNIC™ software package was used for the spectra processing.

2.6. MAS NMR spectroscopy

Solid-state NMR experiments were performed using Bruker Avance III spectrometer operating at 20.0T using a specially designed Doty probe optimized for ^{11}B signal observation and equipped with a "boron-free" stator ensures the acquisition of spectra completely representative of the sample and free from probe signal. The spectra were acquired at an observation frequency of 272.8 MHz for ^{11}B and at a MAS frequency 18.4 kHz after a short excitation pulse to ensure homogeneous irradiation of boron species. The recycling delay was fixed at 5 s and number scans were 256. The ^{11}B chemical shifts were referenced relative to a BF_3OEt_2 solution. In order to determine the chemical shift and line width, the MAS NMR spectrum is fitted using the Dmfit software [18].

3. Results and discussion

3.1. Initial observations and weight changes

The both parts of the samples – immersed in the melt and the part above the bath level – were evaluated and compared with un-corroded specimen Fig. 3. Occasional pitting corrosion attack was found on the immersed parts of the samples, regardless the holding time. The parts of the samples exposed just to the gas corrosive environment showed no visible corrosion attack.

Small weight increase after the tests was observed on the samples at all applied exposure times. The values of weight increase have been in the range 1.3–6.5% (average ca 4%), regardless the holding time. The weight increase was caused by melt penetration into the open superficial pores. Due to interaction between the melt and the TiB_2 substrate, we were not able to remove this melt even after a repeated application of the cleaning procedure. The powder XRD analysis of the solidified corrosion medium (after 200 h of corrosion exposition time) was also carried out Fig. 4. The major identified crystalline phases are $KAlF_4$ and K_3AlF_6. Both species are product of the reaction between the constituents of the melt [1,19].

The XRD patterns of the solidified melts also show one unknown peak at $2\Theta = 13.22^{\circ}$, which was not possible to assign (based on PDF2 database) to any known species. Due to the high intensity of that peak, we expect, that it does not come from TiB_2. We assume that this peak is rather related to the present of special type of alumina (potassium doped alumina) in the solidified melt. A similar behaviour of alumina (in this case doped by sodium) was also observed in the system $NaF-AlF_3-Al_2O_3$ [22–24].

3.2. SEM-EDX and EBSD cross-section analysis

For the better understanding of corrosion mechanism on the interface between the substrate and the melt, a cross-sectional SEM-EDX elemental mapping and EBSD analysis have been carried out on the uncleaned samples. The analysis was focused primarily on the places on the surface where the samples were covered by the melt, thus the solidified melt was still visible. The Fig. 5 shows a photograph of the cross-section of the TiB_2 sample after 200 h of exposition. A SEM-EDX analysis was later performed on the surface of the sample denoted on Fig. 5 as area A and B.

The central part of Fig. 5 shows an exposed part of the TiB_2 sample. One can notice there a drifting of the grains from the surface of TiB_2 material into the melt. (This feature is characteristic for all the TiB_2 samples, regardless the exposition time.) As it can be seen from Fig. 5,

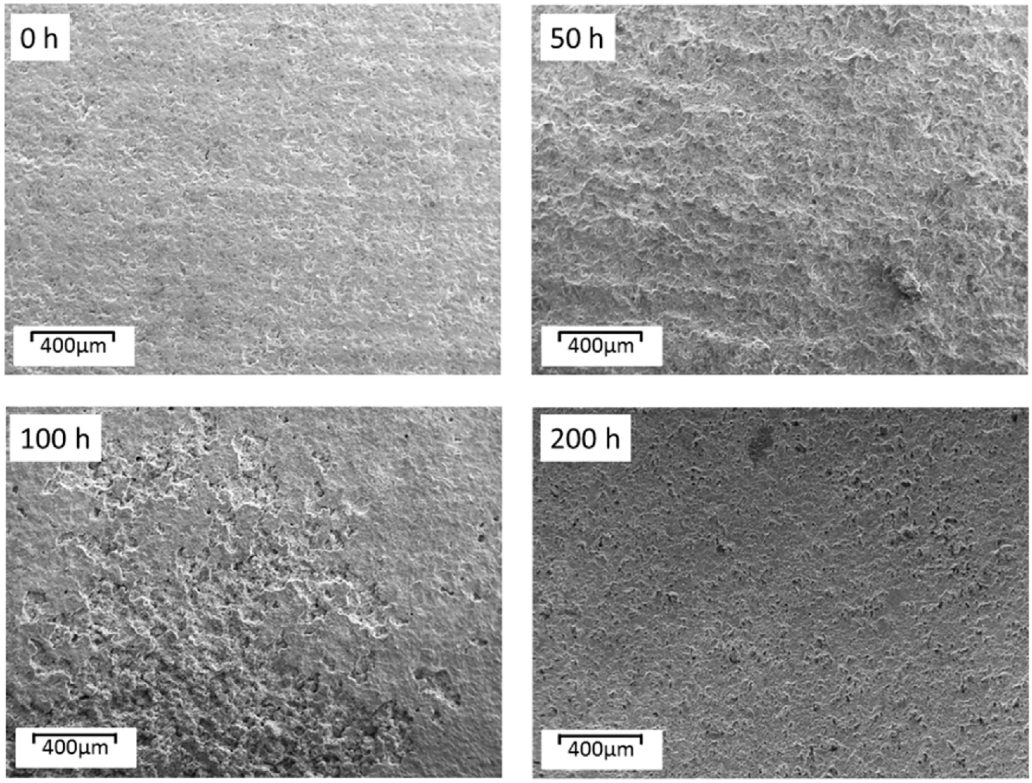

Fig. 3. TiB_2 surface: from left, un-corroded surface, surface after 50 h, 100 h and 200 h of exposure in the melt $KF-AlF_3-Al_2O_3$: 54.8-42.1-3.1 mol% (CR = 1.3).

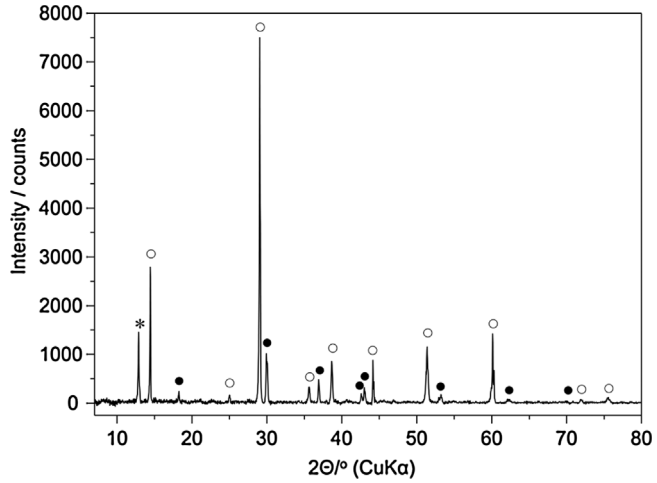

Fig. 4. A XRD pattern of the solidified melt ($KF-AlF_3-Al_2O_3$: 54.8-42.1-3.1 mol%) after 200 h of exposition; ○ – $KAlF_4$ (JCPDS 84–1009) [20], ● – K_3AlF_6 (JCPDS 29-0010) [21], ∗ – potassium doped alumina [22–24].

we have identified the corrosion layer (thickness is around 200 μm), where the TiB_2 material is affected by the penetration of the melt. The penetration continuously decreases from the edges of the attacked area, where the grains of TiB_2 are less affected by the corrosion, to the bulk of the material, completely unaffected by the corrosion (Fig. 5 – far-off left side). Having seen the results of the EDX analysis (Fig. 6.), one can conclude that the corrosion process starts by the penetration of the melt into the pores of the TiB_2 material. The melt then reacts with the intergranular phase and with the TiB_2 grains itself. The cross-sectional EDX analysis confirmed that statement. The grains of the TiB_2 material in the corrosion layer (area A) are attacked by inter-crystal and *trans*-crystal corrosion (Fig. 6B). These parallel corrosion attacks led to a gradual dissolution of the intergranular phase in to the melt, which results to a "liberating" of TiB_2 grains in to the melt. The consequence of that is a drifting of the grains on Fig. 5, from the surface of TiB_2 material, more into the bulk of the solidified melt.

A SEM-EDX analysis was also realized on certain places on the cross-section of the sample with the highest exposition time in order to estimate the chemical processes that could take place on the interface between the grains, melt and the intergranular phase. (Fig. 7a).

We have performed the SEM-EDX on three type of places on the sample: in the bulk of the TiB_2 grains (point 1 and 2); on the interface between the grain and the intergranular phase (points 3–6); and in the bulk of intergranular phase (point 7 and 8).

The single point analysis of the bulk of TiB_2 grains, in both parts, immersed in the melt and exposed to the vapours (point 1 and 2 in Table 2 and Fig. 7), shows that the results exactly corresponds to the original TiB_2 phase. The boundaries of TiB_2 grains are, however, visibly attacked by the melt (points 3–6). This boundary area contains K, Al, F, Ti and O, with significantly higher concentration of aluminium, oxygen and fluorine, in particular. The analysis also showed that boron, on the other hand, completely disappeared from the analysed places on the interface between grains and the melt (points 3–6, in both cases, Fig. 7A and B). The explanation of this observation is based on the fact that during the corrosion test, the melt interacts with the grains resulting the breaking of the Ti–B bonds and thus leaching boron in to the melt.

Decreased content of boron, or its absence in the grains at the surface region attacked by melt, was observed by SEM EDS analysis. The presence of oxygen instead of boron was detected in the grains, dislodged from the surface. We assume, that the mechanism of corrosion is related to gradual dissolution and disintegration of intergranular phase. This mechanism was similar in both cases: for sample in direct contact with the melt, as well as, for the parts, just exposed to the melt's vapours. The only difference was, that, in the case of vapours, the dislodging of TiB_2 grains did not take place. Boron in TiB_2 was partially or completely substituted by oxygen, presented in the melt from dissolving alumina. Higher bonding energy between Ti and O (672 kJ × mol^{-1}) than between Al and O (511 kJ × mol^{-1}) could have been responsible for that preferential formation of titanium oxides [25].

The intergranular phase before the corrosion tests consisted just of

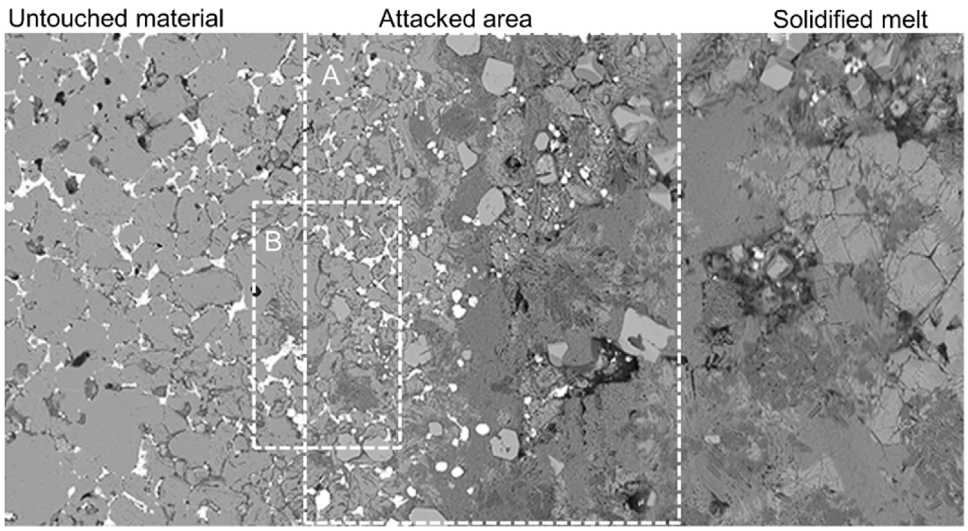

Fig. 5. A cross-section of the TiB_2 sample after 200 h of exposition. On the left – TiB_2 sample, on the right – melt $KF-AlF_3-Al_2O_3$: 54.8-42.1-3.1 mol%; Middle part: as area A and area B, where SEM-EDX analysis was taken (Fig. 6).

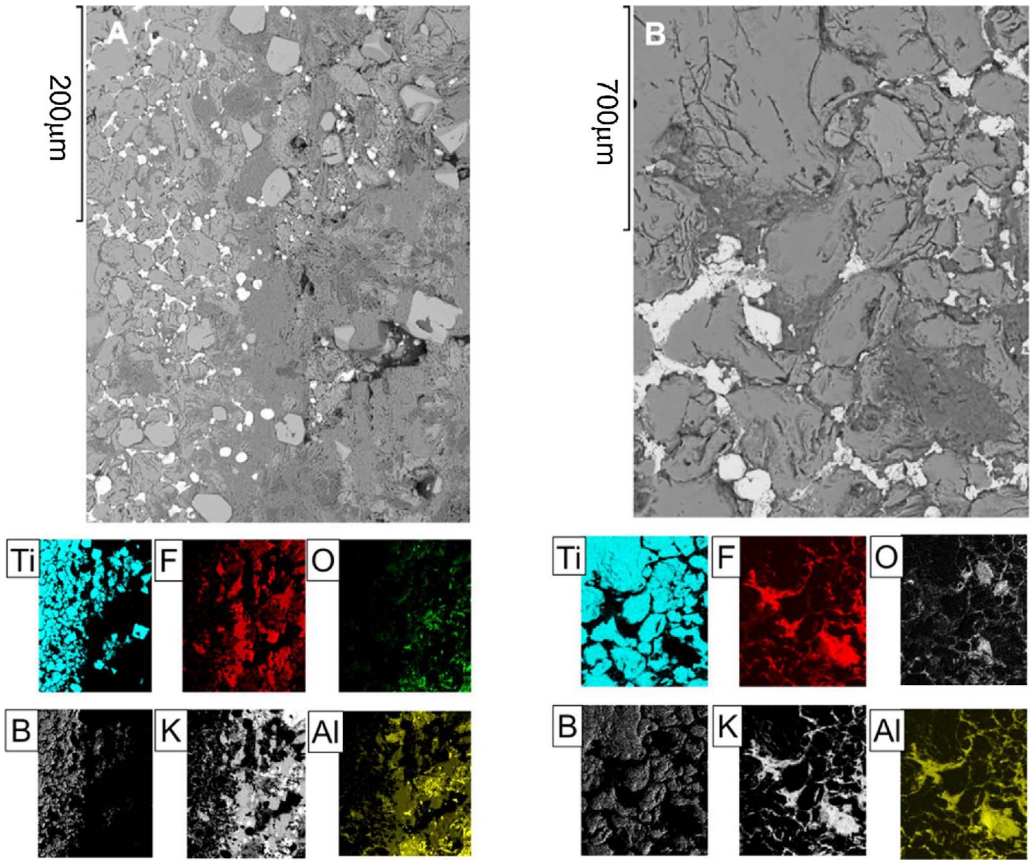

Fig. 6. A cross-section view and SEM-EDX elemental map of the TiB_2 sample after 200 h of exposition in the melts ($KF-AlF_3-Al_2O_3$: 54.8-42.1-3.1 mol%).

Ni, Ti and B. This phase also interacted with the melt, which could be seen in high Ni content, identified by SEM in the point 7 and 8 (Table 2: point 7 and 8). The elemental analysis showed the presence of all the elements, except that of boron. The attacked intergranular phase had however a higher content of oxygen in comparison with the attacked grain boundary. The results of SEM-EBSD are consistent with the SEM-EDX analysis and it confirms the proposed oxidation of the TiB_2 grains (formation of TiO_2), that were in contact with corrosion medium. Blue areas in Fig. 8 represent TiO_2 with "brookite" type of orthorhombic structure, while the red areas represent the TiB_2 grains. Other areas in the picture are not indexed, likely due to the practical impossibility to homogeneously polish composite surfaces of the samples.

There are several possibilities for the behaviour of boron from TiB_2 grains during the corrosion tests:

- Boron evaporates from the system, most likely in the form of gaseous BF_3(g);
- Boron remains in the system in different possible type of species.

In order to answer these questions and to facilitate the identification of boron-containing products, simple experiments with the melt containing 5 wt.% of a TiB_2 powder was performed. The original mixture of corrosion medium ($KF-AlF_3-Al_2O_3$: 54.8-42.1-3.1 mol%) with the 5 wt.% of TiB_2 powder was homogenized and melted at 680 °C in Pt crucible. The sample was held at this temperature during 120 min and cooled down to room temperature spontaneously.

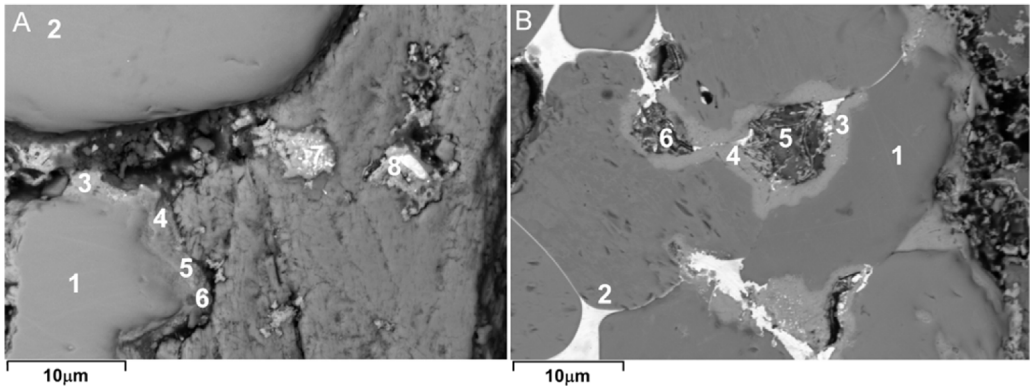

Fig. 7. A SEM image of the cross-section of TiB_2 sample immersed in melt (A) and exposed to vapours of corrosion medium (B) for 200 h.

Table 2
The content of individual elements (values in atomic%) in the cross-section of the TiB2 sample after 200 h corrosion obtained by SEM-EDX single point analysis. Fig. 7(A) - sample immersed in the melt, Fig. 7(B) - parts exposed just to melt`s vapours.

Fig.7A	K	Al	F	O	Ti	B	Ni	Total*
Point								
1	–	–	–	–	29.1	70.9	–	100
2	–	–	–	–	32.4	67.6	–	100
3	0.3	7.4	9.2	50.1	32.8	–	–	99.8
4	0.9	9.6	13.3	40.7	35.3	–	–	99.8
5	1.2	11	14.3	40.7	32.3	–	–	99.5
6	1.9	13.2	17.9	37	29.4	–	–	99.4
7	2	8.1	6.9	21.1	42.1	–	19.2	99.4
8	1.2	8.9	7.9	24.4	41.7	–	15.3	99.4
Fig.7B	K	Al	F	O	Ti	B	Ni	Total*
Point								
1	–	–	–	–	30.3	69.7	–	100
2	–	–	–	–	31.5	68.5	–	100
3	0.7	3.5	2.5	49.5	43	–	–	99.2
4	0.5	4.2	2.9	52.8	37.5	–	1	98.9
5	1	5.2	2.9	47.4	42	–	–	98.5
6	1.3	5.6	2.8	55.5	33.2	–	–	98.4

* Difference from 100% is minor content of impurities (Si, Ca, Na, etc.).

In the first step, we have tested an evaporation of boron species from the melt. We did two parallel experiments, with and without the TiB_2 powder in the mixture. Although, we have seen some weight losses after the melting, there was no difference in weight loses in between two parallel experiments, indicating that boron species did not participate on the evaporation and they should remain presence in the melt. The weight́s loses, observed in both parallel experiments, are likely due to the following reaction 1.

$$KF(l) + AlF_3(s) = KAlF_4(g) \quad (1)$$

The solidified mixture with higher concentration of TiB_2 was, then, also, analysed by several spectral techniques. We now turn to the results and discussion of this analysis.

3.3. Spectral analysis of the solidified mixture with higher concentration of TiB_2

3.3.1. X-ray diffraction

The sample itself, after the solidifying, was clearly composed of two components. The major part was the bulk (core in the centre of the solidified samples), the second was an elevated film on the wall of the Pt crucible. We have analysed both part separately. XRD analysis of the bulk revealed, that this part of the samples also contained, besides the initial TiB_2, some new phases. The major one was attributed to $KAlF_4$, the rest was K_3AlF_6 and TiO_2. We have not seen there any other boron containing species, nor Al_2O_3.

The XRD analysis of the elevated film layer is depicted on Fig. 9. All major diffraction peaks can be indexed to K_3AlF_6 (JCPDS 29-0010) [21] and $KAlF_4$ (JCPDS (84–1009) [20]). The rest of the visible reflection at 16.4° can be indexed to mullite (orthorhombic system, *hkl*: 110; 2Θ-CuKα: 16.4°) [26,27], which is the most intense reflection of so-called boron-mullites [28–30].

This type of aluminium borates represents very important class of materials with great industrial importance. During ongoing research related to the properties of amorphous solids belong to the system $Al_2O_3-B_2O_3$, the authors observed that, after proper heat treatment, solids comprised of between 15 and 50% B_2O_3 do generate a unique series of mixed crystals, whose XRD patterns are perfectly comparable to those of the above-mentioned mullite-like phases, as well as to that of ordinary silica-containing mullite [28]. The term “boron-mullite” or “B-mullite” was first time introduced by Werding and Schreyer in 1984 [31]. The end-members of B-mullites at Al-borates are Al_2O_3-rich aluminoborate type of Al_5BO_9 (Al5B1, i.e. $5Al_2O_3{\cdot}1B_2O_3$) and $AlBO_3$ (Al1B1), respectively [32]. The other compounds in the composition range for “boron-mullites” are: $Al_{18}B_4O_{33}$ (Al9B2); $Al_8B_2O_{15}$ (Al4B1); Al_3BO_6 (Al3B1), and $Al_4B_2O_9$ (Al2B1) or their solid solutions [29].

The Al_2O_3-rich aluminoborate types are typically crystals with orthorhombic symmetry. The octahedral AlO_6 chains are linked by a complex array of polyhedra: AlO_5 bipyramids, AlO_4 tetrahedra and one kind of BO_3 triangles [29]. Mazza et al. [28] describe crystal structures of the Al_5BO_9. They described the structure in space group *Cmc*21, consisting of mullite-type octahedral AlO_6 chains, linked by edge-sharing AlO_5 bipyramids alternating with AlO_4 tetrahedra and BO_3 triangular units. Fischer and Schneider assigned this compound to the “MUL-VIII.33, Bb21m: A9B2” group, together with next one in composition range, $Al_{18}B_4O_{33}$ (Al9B2) [29]. These mullite-type compounds predominantly have 3-coordinated boron but the other ones, at the low alumina content, have additional boron in tetrahedral coordination. It should be noted, that replacing Al_2O_3 with B_2O_3 increases BO_4 content in boron-mullites.

Mazza et al. [28] studied the substitution series of phases between Al_5BO_9 (Al5B1) and $Al_4B_2O_9$ (Al2B1) ones. Their crystal structure refinement, supported by IR studies, showed that boron resides in BO_3 groups in the high-alumina (B-poor) compound and partially substitutes for Al in the tetrahedral position in addition to the formation of BO_4 groups in the low alumina (B-rich) compound. It was confirmed, that the crystal structure of $Al_4B_2O_9$ have a monoclinic symmetry, in which the octahedral AlO_6 chains are cross-linked by AlO_4 groups, BO_4 tetrahedra, BO_3 triangles, and AlO_5 bipyramids [29]. Thus, Al occurs in tetrahedral, bipyramidal and octahedral coordination. Boron has two co-ordinations, classical BO_3 and tetrahedral BO_4, respectively. In order to be able to distinguish what kind of boron-mullite type is going to about in our case, a FT-IR and ^{11}B MAS NMR analysis were applied.

3.3.2. FT-IR characterization

FT-IR spectroscopy has been applied for studying the vibrational

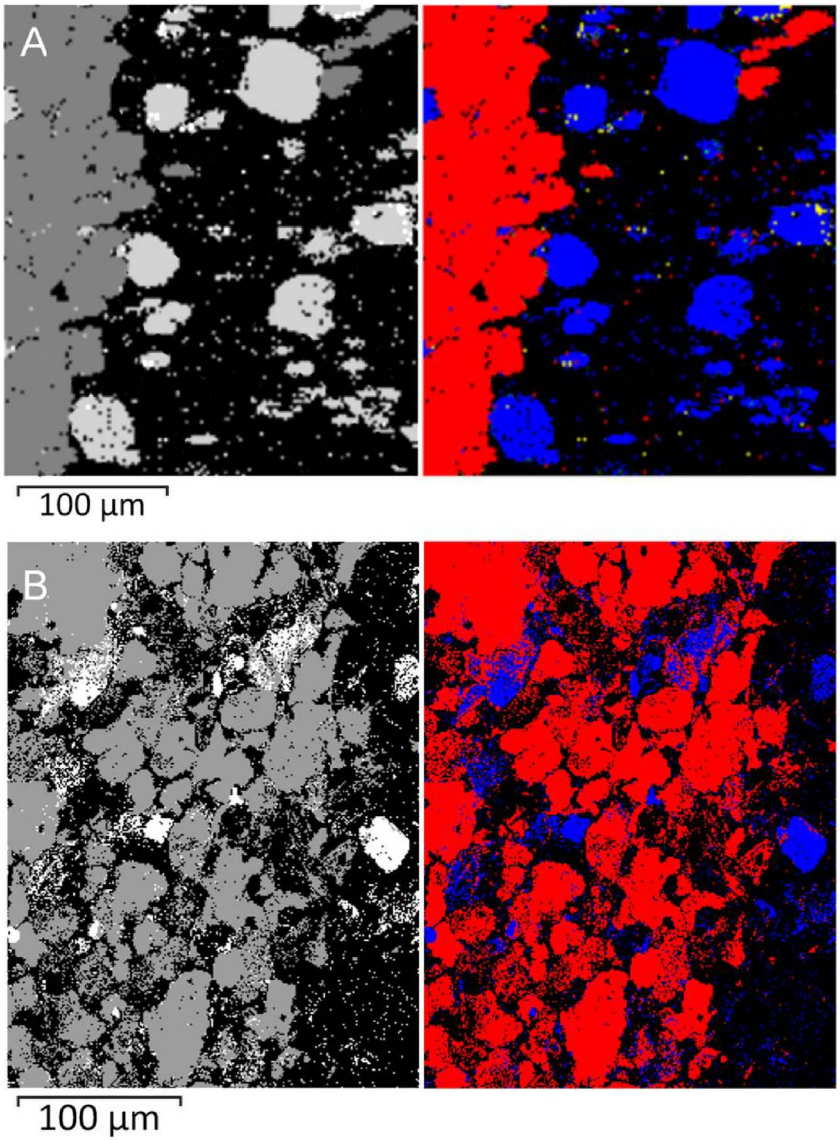

Fig. 8. EBSD phase maps of the corrosion layer of TiB_2 sample after 200 h exposure in the melt, $KF-AlF_3-Al_2O_3$: 54.8-42.1-3.1 mol%. Grains dislodged from the material (a), main corrosion layer (b). Blue – TiO_2, red – TiB_2. (For interpretation of the references to colour in this figure legend, the reader is referred to the web version of this article.)

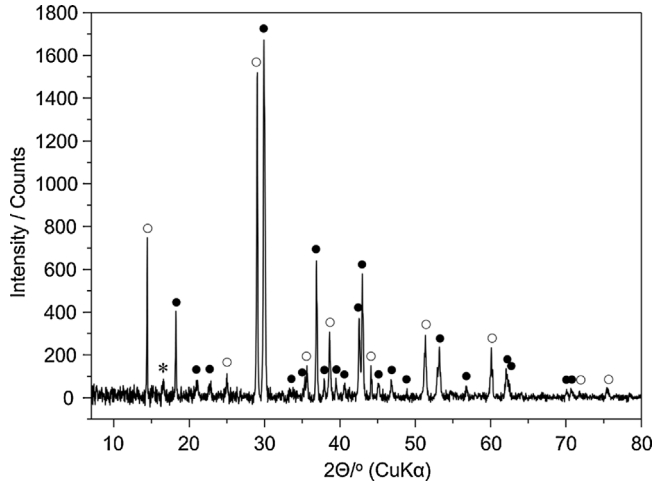

Fig. 9. A XRD analysis of the solidified sample with 5 wt.% of a TiB_2 powder, elevated film; ○ – $KAlF_4$ (JCPDS 84–1009) [20], ● – K_3AlF_6 (JCPDS 29-0010) [21], ∗ – "Boron-mullite" phase [26–30].

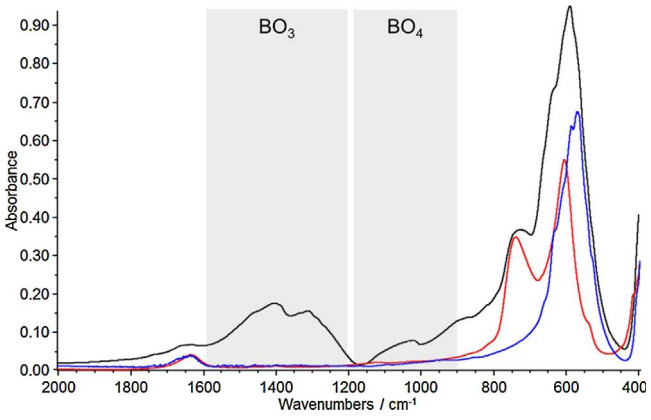

Fig. 10. FT-IR analysis of the solidified sample with 5 wt.% of a TiB_2 powder, elevated film; black line – analysed sample, red line – $KAlF_4$ [33], blue line – K_3AlF_6 [34]. (For interpretation of the references to colour in this figure legend, the reader is referred to the web version of this article.)

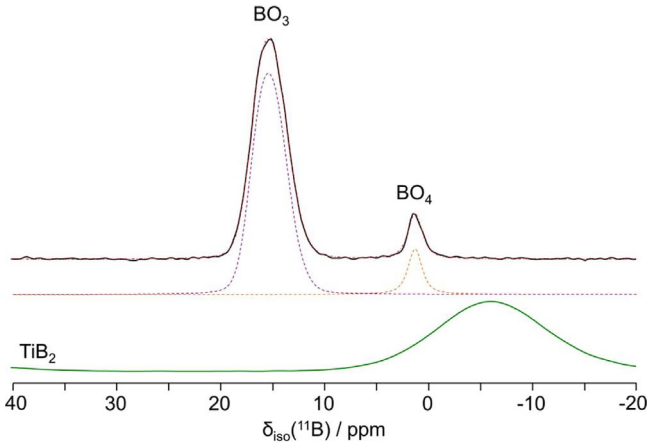

Fig. 11. Experimental (black) and simulated (red) 11B single pulse MAS NMR spectrum of sample at Bo = 20T, and at 18.4 kHz MAS; and fitted profile (color lines). In green are the expansions of the 11B MAS spectra in the region of the central transition of TiB2. (For interpretation of the references to colour in this figure legend, the reader is referred to the web version of this article.)

properties of investigated sample in the spectral range of 400–4000 cm^{-1}. The FT-IR spectrum is depicted in Fig. 10.

The spectra were recorded on KBr pressed disks. A small intense band at 1633 cm^{-1} is precisely due to the bending of H−O−H vibrations from residual moisture from KBr.

The overlapping signals in the region 800–400 cm^{-1} belong to Al−F vibrations in $KAlF_4$ and K_3AlF_6, respectively. The dominant strong signal composed of several overlapping signals belongs to distinct deformation vibrations of AlF_6 octahedra of $KAlF_4$ and K_3AlF_6, respectively. Moreover, the symmetry of these vibrations can be lowered, providing a splitting of these fundamental vibrations. The result is a sequence of vibrations and shoulders at 634 cm^{-1}1, 605 cm^{-1}, 588 cm^{-1}, and 572 cm^{-1}. The band at 730 cm^{-1} might have been left from the bridging of AlF_6 octahedra in $KAlF_4$ [33,34].

The signals in the region from 900 to 1600 cm^{-1} belong to vibrations, which region is characteristic for the presence of typical vibrational modes of borate structural units such as symmetric BO_3 triangles, BO_4 tetrahedrons, and asymmetric BO_3 units (non-bridging oxygen) [28]. In this region, the spectrum of the analysed sample displays a very strong overlapping signal with vibration bands first centred at 1310 cm^{-1}. That is typical for the triangular borate ion BO_3 (BO asymmetric stretching).

The second vibration band centred at 1410 cm^{-1} is assigned to the stretching vibrations of the same BO_3 units [35]. The shoulder, at 1285 cm^{-1}, is related to the asymmetrical O−B−O bonds. The bending motions of the BO_3 group and all other vibrations of the AlO_x polyhedras (including lattice vibrations) are contained in the complex band region between 900 and 100 cm^{-1}. Because of overlapping with more intense Al−F vibrations, these vibrations will not be discussed.

The characteristic IR-active antisymmetric stretching bands of the BO_4 tetrahedron are usually observed in vibrational region at 1200–900 cm^{-1}. Therefore, the weak broad band in our spectrum at around 1020 cm^{-1} was assigned to antisymmetric stretching modes of the BO_4 tetrahedron.

It can be concluded, that our sample could contain boron in both coordinations, BO_3 and BO_4, respectively. This means that our sample could contains a boron-mullite structure, where Al_2O_3 is in low concentration. Our spectra, in the range between 1600 and 1000 cm^{-1}, are about to very similar to those observed by Vitanov et al. [35], were, in the mixture $Al_2O_3-B_2O_3$, 26% of Al is replaced by boron. The final composition then could be written as: $(Al_2O_3)_{0.74}\cdot(B_2O_3)_{0.26}$, (Al2.85B1).

3.3.3. ^{11}B MAS NMR

The presence of four coordinated boron in our sample is clearly supported by the results of ^{11}B MAS NMR spectrum, presented on Fig. 11.

The signal, clearly corresponding to the trigonal boron environment BO_3 [30,36], is broader and exhibits the characteristic lineshape of a quadrupolar nucleus ($I(^{11}B) = 3/2$) blunt by a chemical shift distribution (δ_{iso} = 17.6 ppm; C_Q = 2.8 MHz; Δ_{CS} = 2 ppm). This resonance has been simulated using a line shape taking into account a second order quadrupolar interaction as well as a slight chemical shift distribution. In contrast to that, BO_4 units are typically characterized by resonances at more negative chemical shifts, in region from −4 to 2 ppm30,32. The resonance attributed to the symmetric BO_4 can be simulated by a narrow Lorentz/Gauss lineshape centred at 1.3 ppm with a Full Width at Half Maximum (FWHM) of 350 Hz. This spectrum has revealed no presence of titanium diboride in measured sample and it confirms our SEM-EDX results.

4. Conclusions

A microscopic analysis has revealed that only a few signs of slight corrosion has been observed after the corrosion tests in KF–AlF_3–Al_2O_3 (54.8-42.1-3.1 mol%) melt, at 680 °C. An occasional pitting corrosion has been found on the immersed spots of the samples, regardless the holding time. Small weight increase after the tests was also observed, due to a penetration of the corroding medium in to the open superficial pores of TiB_2.

The interaction between the material and the melt results into surface degradation. The gradual dissolution of Ni-containing grain boundary phase has resulted in the dislodging of TiB_2 grains and their gradual drift into the melt. The edges of TiB_2 grains were also attacked by the melt, resulting in the breaking of Ti–B bonds and thus leaching boron in to the melt. ESBD analysis has showed that a brookite type of the orthorhombic formation of TiO_2 take place on the attacked grains. The XRD, FT-IR and 11 B MAS NMR analysis of the solidified melt has shown that boron is present there (after the corrosion test) in the form of alumina-borates, with the composition $(Al_2O_3)_{0.74}\cdot(B_2O_3)_{0.26}$.

Acknowledgements

This work was supported by the Slovak Grant Agency (VEGA 2/0116/14 and VEGA 2/0114/16) and by the Slovak Research and Development Agency under the contract No. APVV-15-0738 and APVV-15-0479.

References

[1] P. Fellner, G.M. Haarberg, J. Híveš, H. Kvande, A. Sterten, J. Thonstad, Aluminium Electrolysis Fundamentals of the Hall-Héroult Process, 3rd ed., Aluminium Verlag GmbH, Dusseldorf, 2001.
[2] A.L. Yurkov, Refractories and carbon cathode materials for the aluminum industry, Refract. Ind. Ceram. 47 (3) (2006) 139–145.
[3] M. Sørlie, H.A. Øye, Cathodes in Aluminium Electrolysis, 3rd ed., Aluminium-Verlag Marketing & Kommunikation GmbH, Düsseldorf, 2010.
[4] R.P. Pawlek, Aluminum wettable cathodes: an update, Light Metals (2000) 449–454.
[5] R.P. Pawlek, Wettable cathodes: an update, Light Metals (2010) 377–382.
[6] Q. Li, Y. Lai, J. Li, J. Yang, J. Fang, Z. Chen, The effect of sodium-Containing additives on the sodium penetration-Resistance of TiB2/C composite cathode in aluminium electrolysis, Light Metals (2005) 789–791.
[7] Y. Hengwei, L. Wangxing, Q. Shilin, L. Ji, Corrosion resistance of cathode to NaF-KF-AlF_3 based. electrolyte, Light Metals (2010) 855–858.
[8] J. Thonstad, E. Olsen, Cell operation and metal purity challenges for the use of inert anodes The Journal of The Minerals, Metals Mater. Soc. 53 (5) (2001) 36–38.
[9] R.P. Pawlek, Inert anodes: an update, Light Metals (2002) 449–456.
[10] R.P. Pawlek, Inert anodes: an update, Light Metals (2008) 1039–1045.
[11] J. Yang, J.N. Hryn, G.K. Krumdick, Aluminum electrolysis tests with inert anodes in KF-AlFs-Based electrolytes, Light Metals (2006) 421–424.
[12] M.S. Jensen, M. Pezzotta, Z.L. Zhang, M.-A. Einarsrud, T. Grande, Degradation of TiB_2 ceramics in liquid aluminum, J. Eur. Ceram. Soc. 28 (2008) 3155–3164.
[13] Z. Wang, Y. Ban, Z. Shi, B. Gao, D. Lv, Ch. Ma, H. Kan, X. Hu, Penetration of sodium

and electrolyte to vibratory compaction TiB_2 cathode, Light Metals (2008) 1029–1032.
[14] J. Xue, X. Chen, Y. Gao, J. Zhu, Wettability of liquid aluminum on carbon/Graphite/TiB_2 composite cathode materials, Light Metals (2010) 383–386.
[15] V. Pavlík, M. Kontrík, M. Boča, Corrosion behavior of incoloy 800H/HT in the fluoride molten salt FLiNaK + MF_x (MF_x = CrF_3, FeF_2 FeF_3 and NiF_2), New J. Chem. 39 (2015) 9841–9847.
[16] H. Nishimura, T. Terai, M. Yamawaki, S. Tanaka, A. Sagara, O. Motojima, Compatibility of ferritic steels with Li_2BeF_4 molten salt breeder, J. Nucl. Mater. 307-311 (2002) 1355–1359.
[17] Casino: Monte Carlo Simulation of Electron Trajectory in Solids, (2016) Accessed 06 March 2016 http://www.gel.usherbrooke.ca/casino/.
[18] D. Massiot, F. Fayon, M. Campron, I. King, S. Le Calve, B. Alonso, J.O. Durand, B. Bujoli, Z. Gan, G. Hoatson, Modelling one and two-dimensional solid-state NMR spectra, Magn. Reson. Chem. 40 (2002) 70–76.
[19] R. Chen, G. Wu, Q. Zhang, Phase diagram of the system KF–AlF_3, J. Am. Ceram. Soc. 83 (12) (2000) 3196–3198.
[20] A. Gibaud, A. Le Bail, A. Bulou, A re-investigation of the room-temperature phase of $KAlF_4$: evidence of antiphase domains, J. Phys. C: Solid State Phys. 19 (24) (1986) 4623–4633.
[21] A.M. Abakumov, G. King, V.K. Laurinavichute, M.G. Rozova, P.M. Woodward, E.V. Antipov, Crystal structure of (-K_3AlF_6: elpasolites and double perovskites with broken corner-Sharing connectivity of the octahedral framework, Inorg. Chem. 48 (2009) 9336–9344.
[22] P.A. Foster Jr., J. Am. Ceram. Soc. 43 (2) (1960) 66.
[23] P.A. Foster Jr., The system sodium Fluoride—Alumina investigated by quenching methods, J. Am. Ceram. Soc. 45 (4) (1962) 145–148.
[24] M. Kucharík, M. Boča, C. Bessada, H. Fuess, Do sodium oxofluoroaluminates exist at room temperature, Eur. J. Inorg. Chem. 2005 (2005) 1781–1786.
[25] W.M. Haynes (Ed.), CRC Handbook of Chemistry and Physics, 96th ed., CRC Press/Taylor and Francis, Boca Raton, FL, 2016Internet Version 2016.
[26] T. Ban, K. Okada, Structure refinement of mullite by the rietveld method and a new method for estimation of chemical composition, J. Am. Ceram. Soc. 75 (1992) 227–230.
[27] G. Brunauer, H. Boysen, F. Frey, T. Hansen, W. Kriven, High temperature crystal structure of a 3:2 mullite from neutron diffraction data, Zeitschrift fuer Kristallographie 216 (2001) 284–290.
[28] D. Mazza, M. Vallino, Mullite-Type structures in the systems Al_2O_3-Me_2O (Me = Na, K) and Al_2O_3-B_2O_3, J. Am. Ceram. Soc. 75 (7) (1992) 1929–1934.
[29] R.X. Fischer, H. Schneider, Crystal chemistry of borates and borosilicates with mullite-type structures: a review, Eur. J. Miner. 20 (2008) 917–933.
[30] H. Luhrs, The Influence of Boron on the Crystal Structure and Properties of Mullite, PhD Thesis, Universität Bremen, Bremen, Germany, 2013.
[31] G. Werding, W. Schreyer, Alkali-free tourmaline in the system MgO-Al_2O_3-B_2O_3-SiO_2-H_2O, Geochim. Cosmochim. Acta 48 (6) (1984) 1331–1344.
[32] M. Fisch, Crystal Chemistry of Boron-Bearing Mullite-Type Compounds, PhD Thesis, University of Bern, Bern, Switzerland, 2011.
[33] M.J. Reisfeld, Infrared and Raman spectra of the group IIIA hexafluoride ions, Spectrochim. Acta 29A (1973) 1923–1926.
[34] J. Bondam, The infrared absorption spectra of a number of sodium fluoroaluminates in the wavenumber region between 500 and 800 Cm^{-1}, Acta Chem. Scand. 25 (1971) 3271–3276.
[35] P. Vitanov, A. Harizanova, T. Ivanova, T. Dimitrova, Chemical deposition of Al_2O_3 thin films on Si substrate, Thin Solid Films 517 (2009) 6327–6330.
[36] K.J.D. MacKenzie, M.E. Smith, 1st ed., Multinuclear Solid-state Nuclear Magnetic Resonance of Inorganic Materials vol. 6, Pergamon, USA, 2002.